arXiv:1603.01319v1 [nucl-th] 4 Mar 2016

Sensitivity of the fusion cross section to the density dependence of the symmetry energy

P.-G. Reinhard,[1,*] A.S. Umar,[2,†] P. D. Stevenson,[3,‡] J. Piekarewicz,[4,§] V.E. Oberacker,[2,¶] and J.A. Maruhn[5,**]

[1] *Institut für Theoretische Physik, Universität Erlangen, D-91054 Erlangen, Germany*
[2] *Department of Physics and Astronomy, Vanderbilt University, Nashville, TN 37235, USA*
[3] *Department of Physics, University of Surrey, Guildford, Surrey, GU2 7XH, United Kingdom*
[4] *Department of Physics, Florida State University, Tallahassee, Florida 32306, USA*
[5] *Institut für Theoretische Physik, Goethe-Universität, D-60438 Frankfurt am Main, Germany*

(Dated: March 7, 2016)

Background: The study of the nuclear equation of state (EOS) and the behavior of nuclear matter under extreme conditions is crucial to our understanding of many nuclear and astrophysical phenomena. Nuclear reactions serve as one of the means for studying the EOS.

Purpose: It is the aim of this paper to discuss the impact of nuclear fusion on the EOS. This is a timely subject given the expected availability of increasingly exotic beams at rare isotope facilities [1]. In practice, we focus on ^{48}Ca+^{48}Ca fusion.

Method: We employ three different approaches to calculate fusion cross-sections for a set of energy density functionals with systematically varying nuclear matter properties. Fusion calculations are performed using frozen densities, using a dynamic microscopic method based on density-constrained time-dependent Hartree-Fock (DC-TDHF) approach, as well as direct TDHF study of above barrier cross-sections. For these studies, we employ a family of Skyrme parametrizations with systematically varied nuclear matter properties.

Results: The folding-potential model provides a reasonable first estimate of cross sections. DC-TDHF which includes dynamical polarization reduces the fusion barriers and delivers much better cross sections. Full TDHF near the barrier agreee nicely with DC-TDHF. Most of the Skyrme forces which we used deliver, on the average, fusion cross sections in good agreement with the data. Trying to read off a trend in the results, we find a slight preference for forces which deliver a slope of symmetry energy of $L \approx 50\,\mathrm{MeV}$ that corresponds to a neutron-skin thickness of ^{48}Ca of $R_{\mathrm{skin}} = (0.180-0.210)\,\mathrm{fm}$.

Conclusions: Fusion reactions in the barrier and sub-barrier region can be a tool to study the EOS and the neutron skin of nuclei. The success of the approach will depend on reduced experimental uncertainties of fusion data as well as the development of fusion theories that closely couple to the microscopic structure and dynamics.

PACS numbers: 21.60.Jz,25.60.Pj,21.65.Mn,21.10.Gv,26.60.-c

I. INTRODUCTION

Nuclear saturation—the existence of an equilibrium density—is a hallmark of nuclear dynamics. The semi-empirical nuclear mass formula of Bethe and Weizsäcker [2, 3] regards the atomic nucleus as an incompressible liquid drop consisting of two quantum fluids: one electrically charged consisting of Z protons and one electrically neutral containing N neutrons. The nearly uniform density found in the interior of heavy nuclei and the resulting $A^{1/3}$ scaling of the nuclear size with mass number $A = Z+N$ feature among the most successful predictions of the liquid drop model. However, in reality the liquid drop is not incompressible. Thus, it is pertinent to ask how does the liquid-drop energy increase as the density departs from its equilibrium value [4]. Besides being a fundamental nuclear-structure question, the answer to this inquiry is also vital to our understanding of the nuclear equation of state (EOS). The EOS plays a key role in elucidating the structure of exotic nuclei [5], the dynamics of heavy ion collisions [6, 7], the composition of neutron stars [8–11], and the mechanism of core-collapse supernovae [12–14]. As such, the EOS provides a powerful bridge between nuclear physics and astrophysics.

The quest for the nuclear EOS also generates a strong and healthy interplay between theoretical, experimental, and observational research [15]. New measurements drive new theoretical efforts, that in turn uncover new puzzles that trigger even newer experiments and observations. It is the aim of this paper to discuss the impact of nuclear fusion on the EOS. This is a timely subject given the expected availability of increasingly exotic beams at rare isotope facilities [1]. This new frontier will enable reactions of exotic beams with large neutron excess [16] that will provide critical new information on the poorly-known isospin dependence of the EOS [17, 18]. The isospin dependence of the EOS is encoded in the symmetry energy which, in turn, quantifies the energy cost of turning symmetric nuclear matter into pure neutron matter. The density dependence of the symmetry energy has become an active and vibrant area of research as evinced by the

* paul-gerhard.reinhard@physik.uni-erlangen.de
† umar@compsci.cas.vanderbilt.edu
‡ p.stevenson@surrey.ac.uk
§ jpiekarewicz@fsu.edu
¶ volker.e.oberacker@vanderbilt.edu
** maruhn@th.physik.uni-frankfurt.de

recent topical issue devoted exclusively to this topic [19].

A physical observable that is particularly sensitive to the density dependence of the symmetry energy is the neutron-skin thickness of ^{208}Pb [20–23]; the neutron skin is defined as the difference between the root-mean-square radii of the neutron distribution (R_n) relative to that of the proton (R_p). Whereas elastic electron scattering experiments have provided a very detailed map of the proton distribution throughout the full nuclear chart [24–26], a determination of the neutron density has traditionally relied on hadronic experiments that are hindered by large and uncontrolled uncertainties. However, using parity-violating electron scattering—a purely electroweak reaction—the Lead Radius EXperiment (PREX) has provided the first clear evidence in favor of a neutron-rich skin in ^{208}Pb [27, 28]. Given that the weak charge of the neutron is much larger than the corresponding weak charge of the proton, parity-violating electron scattering provides an ideal tool to map the neutron distribution [29]. Since the proton radius of ^{208}Pb is accurately known [26], the determination of the neutron radius by the PREX collaboration has effectively determined the neutron-skin thickness of ^{208}Pb to be [27]:

$$R_{\rm skin}^{208} = R_n^{208} - R_p^{208} = 0.33^{+0.16}_{-0.18}\,{\rm fm}. \qquad (1)$$

Note that experimental error will be reduced by a factor of three (to $\pm$0.06fm) in an already approved experiment "PREX-II" [30].

An accurate measurement of $R_{\rm skin}^{208}$ will significantly constrain the slope of the symmetry energy L, a fundamental parameter of the EOS that is very closely related to the pressure of pure neutron matter at saturation density. The strong correlation between $R_{\rm skin}^{208}$ and L [23, 31] emerges from a simple question: *where do the excess neutrons go?* Placing the 44 extra neutrons in the core is favored by surface tension but disfavored by the symmetry energy, which is larger at the center than at the surface. Conversely, moving the excess neutrons to the dilute surface increases the surface tension but reduces the symmetry energy. In this way, the neutron-skin thickness of $R_{\rm skin}^{208}$ develops from a dynamic competition between the surface tension and L, which represents the difference between the symmetry energy at saturation density and at a lower surface density [18]. In particular, for a "stiff" symmetry energy, namely one that increases rapidly with density, it is energetically advantageous to move most the excess neutrons to the surface where the symmetry energy is low; this generates a thick neutron skin.

Besides PREX-II, the Calcium Radius EXperiment (CREX) has been already approved to measure the weak form factor of ^{48}Ca at the Jefferson Laboratory via parity-violating electron scattering [32]. This purely electroweak measurement will be carried out a momentum transfer of $q \simeq 0.8\,{\rm fm}^{-1}$ that will allow the extraction of the neutron radius of ^{48}Ca with a precision of 0.02 fm. The advantages of such an experiment are many. First, it provides a theoretical bridge between ab-initio calculations that are now possible in the case of ^{48}Ca [33] and density functional theory which is at present the optimal (and perhaps unique) theoretical tool to describe nuclei all over the nuclear chart. Indeed, the strong correlation observed between $R_{\rm skin}^{208}$ and L while likely robust, has been discussed exclusively in the context of density functional theory. Second, a precise measurement of the weak form factor of a medium-mass nucleus such as ^{48}Ca can be carried out at larger momentum transfer where the parity-violating asymmetry is larger. Indeed, the situation in ^{48}Ca is so favorable that the full weak-charge form factor could be measured using parity-violating electron scattering [34]. Together then, PREX-II and CREX provide a powerful complementary set of inputs to nuclear theory. CREX will allow ab-initio models of nuclear structure to be tested which, in turn, will inform density functional theory. These improved energy density functionals may then be used with confidence to interpret the PREX-II measurement and ultimately place stringent constraints on the density dependence of the symmetry energy.

Most studies of the EOS involve infinite or semi-infinite nuclear matter and examine the dependence of the EOS on the underlying parametrization of the energy density functional (EDF) as well as its relation to the macroscopic and macroscopic-microscopic models of nuclear matter [5, 35, 36]. The basic predictions of all models can be characterized by a small number of nuclear matter properties (NMP) commonly defined at the equilibrium state of symmetric matter. Those NMP may be constrained by the rich spectrum of nuclear collective excitations of diverse spin-isospin character [37]. Among the more prominent ones are the isoscalar giant monopole resonance, [38], the isoscalar giant quadrupole resonance [39], and the isovector giant dipole resonance [40]. Lately, the electric dipole polarizability—which is proportional to the inverse energy weighted sum of the isovector dipole response—has received considerable attention because of its strong connection to the density dependence of the symmetry energy [41–47]. Time dependent Hartree-Fock (TDHF) theory in the small amplitude limit and equivalently the random-phase-approximation (RPA) approaches provide the means for a consistent calculation of these collective excitations [4, 48–58].

Complementing these small-density collective excitations are the large amplitude modes associated with fusion and fission, which provide a challenging testing ground for theoretical models against a vast amount of existing experimental information. For its relevance to CREX, in this paper we limit our study to ^{48}Ca+^{48}Ca fusion. The main goal of such a study is to explore the sensitivity of the fusion cross section to the EOS, particularly to the slope of the symmetry energy which has a strong impact on the thickness of the neutron-rich skin of ^{48}Ca. Although theoretical models of nuclear fusion may be hindered by hadronic uncertainties, sub-barrier fusion is attractive because of the exponential character

of quantum-mechanical tunneling. Indeed, we conjecture that sub-barrier fusion should be significantly enhanced for those models that predict a stiff symmetry energy and consequently a large neutron-skin thickness in ^{48}Ca. To test this conjecture and to explore the sensitivity of the fusion cross section to the EOS we use a series of Skyrme EDFs with systematically varied NMP [59]. We note in passing the close connection between the fusion of two neutron-rich nuclei and the merger of two neutron stars. Indeed, the late inspiral phase of neutron-star mergers probes the nuclear EOS through the tidal deformation of the star which is highly sensitive to the stellar radius. Both the thickness of the neutron skin and the radius of a neutron star have the same origin: the pressure of neutron-rich matter. Hence, models with thicker neutron skins often produce neutron stars with larger radii [60–62]. This interesting correlations provides a compelling connection between nuclear physics and astrophysics.

The paper has been organized as follows. In Sec. II we discuss the general features of the parametrization of the EOS, with a more detailed discussion left to Appendix A. This is followed in Sec. III A by the calculation of fusion barriers using the double-folding potential approach to examine the impact of NMP on fusion cross-sections using a purely static approach. The impact of the dynamics is studied utilizing the density constrained TDHF and direct TDHF calculations in Secs. III B and III C, respectively. A summary of our main findings and some concluding remarks are given in Sec. IV.

II. ENERGY DENSITY FUNCTIONALS

Despite significant progress in nuclear ab-initio calculations (for reviews see e.g. Refs. [63–67]), the predictions are not yet sophisticated enough to serve as the basis for high-precision functionals, especially in the case of medium to heavy nuclei. Consequently, most nuclear EDFs are calibrated to experimental data. The limited availability of discerning data—especially in the case of the isovector sector—as well as approximations and theoretical biases leads to residual uncertainties in the fitted parametrizations and these propagate to uncertainties in the model predictions; for extensive discussions of error propagation and error estimates see, e.g., Refs. [4, 5, 68–72]). It is our aim here to explore the sensitivity and variance of model predictions for fusion cross sections.

From the great variety of nuclear EDFs, we concentrate here on the widely used Skyrme EDFs as a prototype example. The Skyrme force as an effective nuclear interaction dates back to the original work of Skyrme [73] which was then utilized in a quantitative manner in the pioneering paper of Vautherin [74]. The Skyrme interaction was subsequently developed as to provide an accurate description of nuclear structure and dynamics across the full chart of the nuclides [75]. For the purpose of the present study, we focus on the series of Skyrme parametrizations with systematically varied NMP developed in Ref. [59]. The critical point exploited here is that there is a one-to-one correspondence between NMP and the volume properties of the Skyrme EDF. This allows the use of NMP to conveniently characterize each EDF. The calibration of the EDF results in predictions that determine the NMP with some uncertainty. The systematic variation of the NMP is done within this uncertainty band. Tracking the trends of an observable along such systemically varied parametrizations results in an uncertainty in the prediction. In turn, such an uncertainty in the prediction dictates the experimental precision that would be needed to better constrain the underlying EDF.

A detailed description of the Skyrme EDF and its relation to NMP may be found in Appendix A. Here, we limit ourselves to summarize the strategy involved in generated systematically varied parametrizations. In all cases, Skyrme EDFs are fitted to the same pool of bulk properties of the nuclear ground state, namely, binding energies, pairing gaps from odd-even staggering, a few selected spin-orbit splittings, and bulk properties of the nuclear charge distribution, such as the root-mean-square radius, diffraction radius, and surface thickness; for more details see [59]. In addition, the fits are further constrained by four nuclear matter parameters: (a) the incompressibility K of symmetric nuclear matter, (b) the isoscalar effective mass m^*/m, (c) the symmetry energy at saturation J, and (d) the Thomas-Reiche-Kuhn sum rule enhancement factor $\kappa_{\rm TRK}$ (for more details see Appendix A). The base parametrization is SV-bas with $K=234$ MeV, $m^*/m=0.9$, $J=30$ MeV, and $\kappa_{\rm TRK}=0.4$. These NMP are chosen such that the underlying SV-bas parametrization provides a good description of various giant resonances and the electric dipole polarizability in ^{208}Pb. Subsequently, we systematically vary each nuclear matter property by holding all others fixed at their optimal value. Varying K yields SV-K218, SV-K226, and SV-K241, where the corresponding label indicates the adopted value of K. In a similar manner, varying m^*/m yields SV-mas10, SV-mas08, and SV-mas07, corresponding to values of the isoscalar effective mass of $m^*/m = 1.0$, 0.8, and 0.7, respectively. Fixing the symmetry energy at saturation density to $J=28, 32, 34$ MeV yields SV-sym28, SV-sym32, and SV-sym34. Finally, varying $\kappa_{\rm TRK}$ yields SV-kap00, SV-kap20, and SV-kap60, corresponding to values of 0.00, 0.20, and 0.60, respectively. For further details on the predictions of these parametrizations, including the highly uncertain slope of the symmetry energy L, see Table II in Appendix A.

In order to have a better handle on the variation of the neutron skin as a function of the symmetry-energy slope L and its impact on the fusion cross section, we have produced four new forces with dedicated variation of L. To that end, we keep the four NMP fixed as in SV-bas and in addition we set a constraint on L. This constraint is then varied at the unconstrained value of L in a range that still produces reasonable fits. These new forces, labeled "SV-L", are also tabulated in Table II.

In the next section we investigate the trends that

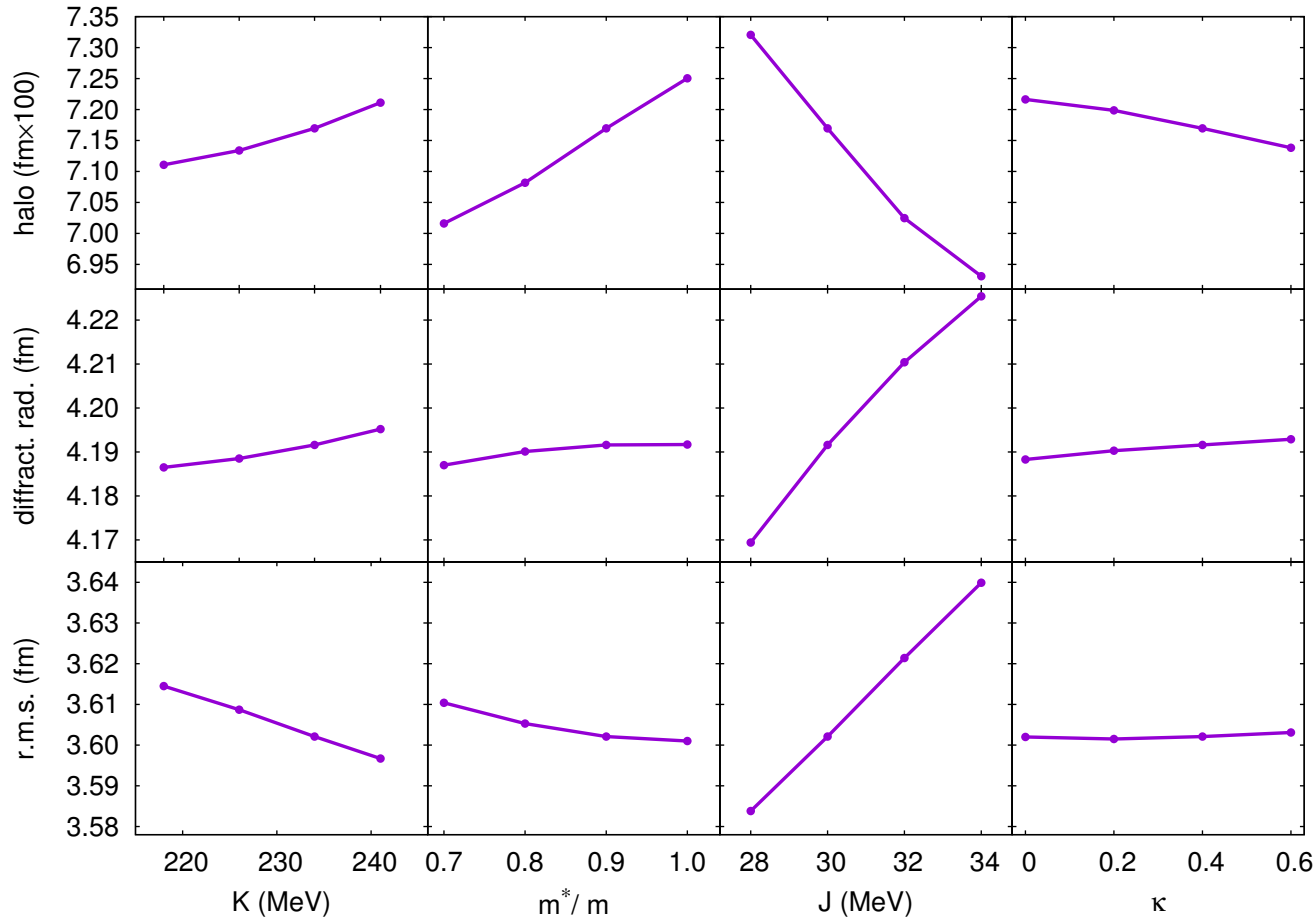

FIG. 1. (Color online) Neutron root mean-square radius (r.m.s.), neutron diffraction radius, and neutron halo of ^{48}Ca obtained from a set of Skyrme parametrizations with systematically varied nuclear matter parameters (incompressibility K, effective mass m^*/m, symmetry energy J, and $\kappa_{\rm TRK}$) [59] for the SV density functionals used in this study

emerge in the fusion barriers and cross sections for the ^{48}Ca+^{48}Ca reaction as we systematically vary the model predictions. Given that we expect that the neutron distribution is the most critical piece determining the nuclear attraction at larger distances, we hope to gain valuable insights into the density dependence of the symmetry energy. In Fig. 1 we show the emerging trends in neutron radii and halo of ^{48}Ca obtained from the series of systematically varied EDFs. As expected, the symmetry energy J has by far the strongest impact on the neutron distribution. In contrast, there is some mild sensitivity of the neutron distribution to the isoscalar effective mass m^*/m and even less to the incompressibility K, and negligble to the sum rule enhancment $\kappa_{\rm TRK}$.

III. FUSION AND NMP

The use of fusion data to elucidate the dependence of cross-sections on NMP requires a deep understanding of the fusion process and its model dependence. Naturally, reducing the highly complex fusion process to the estimation of barrier(s) as a function of the distance between the two nuclei R is a severe simplifying approximation. In order to proceed in this manner, it is critical to test this approximation on various energy regimes, as a function of the properties of the participating nuclei, and on its sensitivity to the microscopic model parameters. For example, in the case of ^{48}Ca one avoids complexities associated with deformation [76] because of the spherical character of this nucleus. The height of the ion-ion interaction barrier is largely determined by the size of the colliding nuclei and their nuclear skin. As the two nuclear surfaces come within the range of the short-range nuclear interaction, the barrier starts to deviate from its purely Coulombic form as a result of the nuclear attraction. In this early stage of the reaction, nuclei gradually developed a so-called "neck", which subsequently evolves into a compound system as the overlapping densities coalesce. For light and mid-mass systems the barrier is found to be largely insensitive to the beam energy [77]. At energies at and above the barrier, the fusion cross-section displays its highest sensitivity to the neutron-skin thickness, which largely determines the height of the barrier. However,

at lower energies the formation of the neck and density rearrangements are expected to be sensitive to the other NMP, such as the incompressibility coefficient and the symmetry energy. The ^{48}Ca+^{48}Ca system shows strong fusion hindrance at deep sub-barrier energies [78]. Sophisticated coupled-channel calculations using the shallow or compression potential approach have been done for this system [79]. These calculations are consistent with a neutron-skin thickness in ^{48}Ca of 0.229 fm based on chosen experimental estimates [26, 80]. Note, that this value is significantly larger than the $R_{\rm skin} \lesssim 0.15$ fm estimate reported recently by Hagen and collaborators using an ab-initio approach [33]. Some of the discrepancy may be due to the fact that the neutron radius of ^{48}Ca quoted in Ref. [80] relies on experiments using elastic proton scattering that are hindered by large and uncontrolled hadronic uncertainties. Fortunately, this situation will improve greatly by a purely electroweak determination of the neutron radius of ^{48}Ca by the CREX collaboration [32]. At this point in our analysis it is not possible to make a robust connection of these results with the EOS and NMP. In addition, the use of frozen densities in calculating the interacting potential is expected to require a slightly larger radius since the early stages of the skin-skin attraction and stretching will occur at a somewhat smaller distance due to the inability of the densities to dynamically stretch.

In this section we employ three different methods to study the dependence of the fusion cross section on the various parametrizations of the Skyrme energy density functional. First, we use the standard double-folding approach to calculate ion-ion potentials using frozen densities. Second, we utilize the density-constrained time-dependent Hartree-Fock (DC-TDHF) approach to calculate the ion-ion potentials directly from TDHF densities. Finally, we perform direct TDHF calculations at above barrier energies to compute the fusion cross sections. In what follows we briefly outline each method and present the associated results.

A. Double-folding potentials

In the double-folding approach the nuclear part of the ion-ion interaction potential is approximated by the so-called double folding potential $V_F(R)$:

$$V_F(\mathbf{R}) = \int d^3r_1 d^3r_2 \rho_1(\mathbf{r}_1)\rho_2(\mathbf{r}_2) V_{NN}(\mathbf{R}+\mathbf{r}_2-\mathbf{r}_1)\,, \quad (2)$$

where $\rho_1(\mathbf{r}_1)$ and $\rho_2(\mathbf{r}_2)$ are the densities of the two nuclei as measured from their respective center of mass and V_{NN} is the effective NN interaction. In practice, we have used self-consistent Hartree-Fock (HF) densities obtained using a spherical Hartree-Fock code and the M3Y effective NN interaction [81–84]. The spherical HF code uses a grid spacing of $dr = 0.3$ fm and maximum radial distance of $R_{max} = 10.5$ fm, which are more than adequate to describe the ground-state density of ^{48}Ca. The double-folding integral is evaluated for the nuclear potential together with the Coulomb integral in momentum space [84]. The double-folding potential is expected to be most reliable for distances where the nuclei begin to touch and, thus, particularly sensitive to the neutron-skin thickness of the colliding ions. At smaller distances, the double-folding potential tends to overestimate the nuclear interaction as a result of the unphysically large overlap density due to the frozen-density approximation.

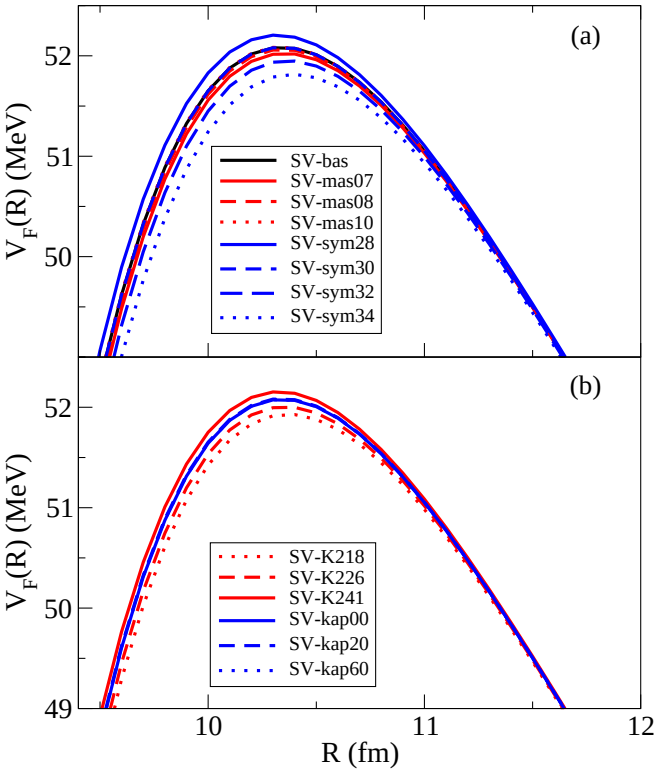

FIG. 2. (Color online) Folding model ion-ion interaction potentials, $V_F(R)$, for ^{48}Ca+^{48}Ca system using the Skyrme SV EDFs; (a) potentials for SV-mas07, SV-mas08, SV-mas10, SV-sym28, SV-sym30, SV-sym32, and SV-sym34. Also shown is the folding potential corresponding to SV-bas. (b) potentials for SV-K218, SV-K226, SV-K241, SV-kap00, SV-kap20, and SV-kap60.

In Fig. 2 we show the ion-ion interaction potentials defined in Eq. 2 for the ^{48}Ca+^{48}Ca system using ground-state densities computed for the set of SV forces defined in Sec.II. In particular, Fig. 2(a) displays the double folding potential as predicted for the following functionals:SV-mas07, SV-mas08, SV-mas10, SV-sym28, SV-sym30, SV-sym32, and SV-sym34. We observe (red lines) that the folding potential is essentially unchanged as the effective mass is varied from 0.7 to 1.0. Instead, we find high sensitivity to the symmetry energy parameter J. The potential peak is largest for the smallest value $J = 28$ MeV and is reduced by as much as 0.5 MeV for SV-sym34, which has $J = 34$ MeV. This finding is consistent with our expectations. A model with a soft symmetry energy (such as SV-sym28) predicts a slow increase in the

energy with increasing density and, consequently a thin neutron skin; in contrast, a stiff symmetry energy generates a thick neutron skin (see Table II). A thick neutron skin enhances the overlap region as the nuclei begin to touch, thereby resulting in a lower Coulomb barrier. And although half an MeV (out of about 50 MeV) may seem as a mild reduction, one must recall that nuclear fusion near the Coulomb barrier depends exponentially on the height of the barrier.

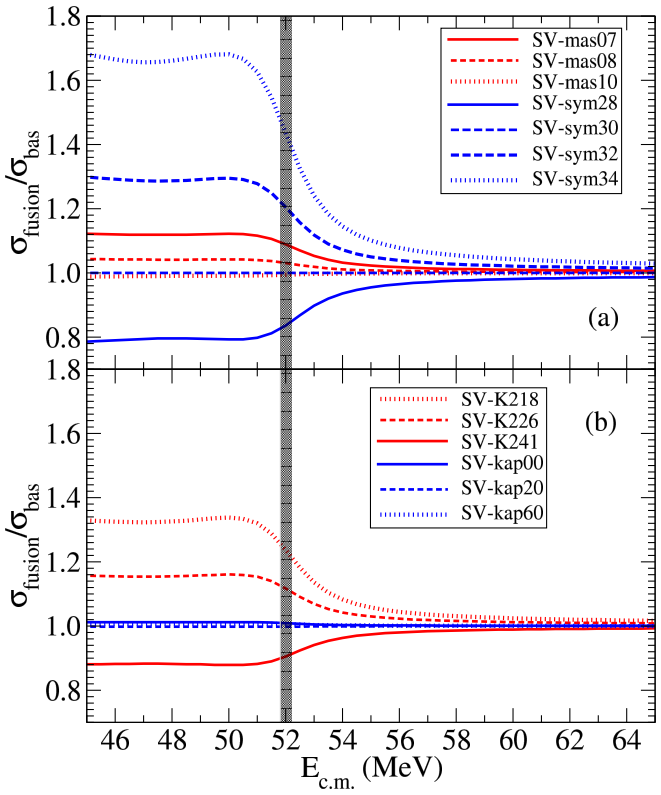

FIG. 3. (Color online) ^{48}Ca+^{48}Ca fusion cross-sections corresponding to the folding model ion-ion interaction potentials $V_F(R)$ for Skyrme SV EDFs, scaled by the fusion cross-section corresponding to the SV-bas barrier. (a) cross-sections ratio for SV-mas07, SV-mas08, SV-mas10, SV-sym28, SV-sym30, SV-sym32, and SV-sym34. (b) cross-sections ratio for SV-K218, SV-K226, SV-K241, SV-kap00, SV-kap20, and SV-kap60. The shaded area indicates the range of folding model potential barrier heights obtained using the SV forces.

The folding potentials corresponding to the systematic variation of the incompressibility coefficient K and the enhancement factor $\kappa_{\rm TRK}$ are now plotted in Fig. 2(b). Here we observe essentially no dependence on $\kappa_{\rm TRK}$ but some sensitivity, albeit small, to K. Larger values of the incompressibility result in a higher potential peak, with the total difference between the highest and lowest peaks being about 0.25 MeV.

As already alluded, these results are fully consistent with the variation of the ground-state properties of ^{48}Ca—especially the neutron r.m.s. radius shown in Fig. 1. Indeed, the bottom row of Fig. 1 clearly indicates that the neutron radius is highly sensitive to the symmetry energy. Given that the folding potential uses frozen densities, the height of the peak is highly sensitive to the extent of the nuclear skin. In particular, SV-sym28, which predicts the smallest neutron radius in ^{48}Ca, generates the highest peak in the potential since the nuclei can reach a smaller ion-ion separation distance R before the outer densities start to overlap. That is, a small neutron skin "delays" the impact of the nuclear attraction to smaller values of R causing an increase in the height of the Coulomb barrier. Moreover, a smaller neutron skin also manifests itself by having the peak in the potential shift to a smaller value of R relative to SV-sym34 which, with the stiffest symmetry energy, generates the largest neutron skin.

We next examine the fusion cross section for the ^{48}Ca+^{48}Ca system interacting via the ion-ion potentials shown in Fig. 2. When the ion-ion collision is reduced to an ion-ion interaction potential dependent on the collective coordinate R the fusion barrier penetrabilities $T_L(E_{\rm c.m.})$ can be obtained by numerical integration of the two-body Schrödinger equation

$$\left[\frac{-\hbar^2}{2\mu}\frac{d^2}{dR^2}+\frac{L(L+1)\hbar^2}{2\mu R^2}+V(R,E)-E\right]\psi(R)=0\,, \quad (3)$$

using the *incoming wave boundary condition* (IWBC) method [85]. The potential $V(R,E)$ is the sum of nuclear and Coulomb potentials. IWBC assumes that once the minimum of the potential is reached fusion will occur. In practice, the Schrödinger equation is integrated from the potential minimum, $R_{\rm min}$, where only an incoming wave is assumed, to a large asymptotic distance, where it is matched to incoming and outgoing Coulomb wavefunctions. The barrier penetration factor, $T_L(E_{\rm c.m.})$ is the ratio of the incoming flux at $R_{\rm min}$ to the incoming Coulomb flux at large distances. Here we implement the IWBC method exactly as it is formulated for the coupled-channel code CCFULL described in Ref. [85]. This gives us a consistent way for calculating cross sections at above and below the barrier via

$$\sigma_f(E_{\rm c.m.})=\frac{\pi}{k^2}\sum_{L=0}^{\infty}(2L+1)T_L(E_{\rm c.m.})\,. \quad (4)$$

To elucidate the sensitivity of the ^{48}Ca+^{48}Ca fusion cross section to the various EDF parametrizations, we have plotted in Fig. 3 the ratio of the calculated cross sections as a function of center-of-mass energy for the potential barriers shown in Fig. 2 relative to the fusion cross section obtained from the base parametrization SV-bas. The top and bottom panels of Fig. 3 correspond to the potentials displayed in the top and bottom panels of Fig. 2. We have adopted the same vertical scale in both panels to emphasize the relative enhancement/quenching factors. The shaded region indicates the range of barrier heights for the potentials shown in Fig. 2. As expected, and fully consistent with our discussion of the potential $V_F(R)$, changes in the symmetry energy have by far the largest

impact on the fusion cross section—particularly below the Coulomb barrier. This is followed by the nuclear incompressibility, which displays a significant dependence, and finally by the effective mass and TRK enhancement factor both displaying minimal impact on the cross section.

We close this section by showing in Fig. 4 the calculated ^{48}Ca+^{48}Ca fusion-excitation function against the experimental data [78]. Note that the exponential nature of quantum-mechanical tunneling below the Coulomb barrier demands the use of a logarithmic scale, as the fusion cross section varies over six orders of magnitude in a 10 MeV interval in center-of-mass energy. Although on such a scale it is difficult to discern significant differences among the predictions of the models, some general trends emerge. Indeed, whereas the model predictions for the cross section above the Coulomb barrier are in reasonable agreement with experiment, the data below the barrier is consistently underestimated. We attribute this discrepancy to the fact that the folding-potential with frozen densities is a poor approximation inside the barrier due to an unphysical density that is grossly overestimated in the overlap region. We note that for c.m. energies above the barrier—where the sensitivity to the neutron-skin thickness ceases to be critical—all SV forces produce similar results, with the cross sections corresponding to SV-sym34 showing the best overall agreement. To provide an improved theoretical description of the cross section and to further examine the sensitivity of the fusion cross section to the underlying SV forces, we relax in the next section the double-folding approximation in favor of a DC-TDHF approach.

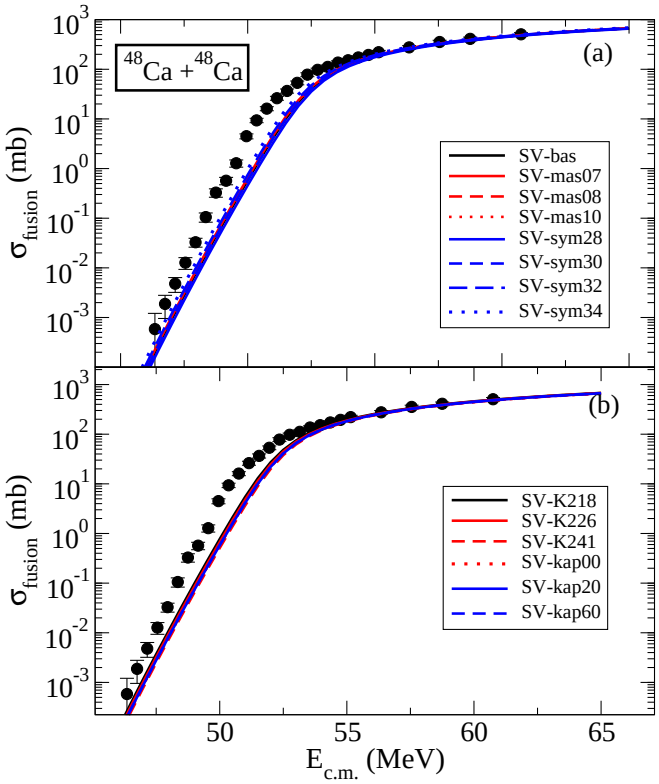

FIG. 4. (Color online) ^{48}Ca+^{48}Ca fusion cross section using an ion-ion interaction $V_F(R)$ obtained in the double-folding approximation with densities computed from the set of systematically varied Skyrme forces. Results are plotted on a logarithmic scale for: (a) SV-mas07, SV-mas08, SV-mas10, SV-sym28, SV-sym30, SV-sym32, and SV-sym34, and (b) SV-K218, SV-K226, SV-K241, SV-kap00, SV-kap20, and SV-kap60. Also shown is the cross section corresponding to SV-bas and the experimental data (filled circles) are taken from Ref. [78].

B. DC-TDHF Method

The folding-model calculations ignore dynamical effects such as neck formation, particle exchange, pre-equilibrium GDR and other modes during the nuclear overlap phase of the reaction. During this phase of the collision the primary underlying mechanism is the dynamical change in the density along the fusion path which modifies the potential energy. Obviously, this density change is not instantaneous. For instance, it was shown in Ref. [86] that the development of a neck due to couplings to octupole phonons in ^{40}Ca+^{40}Ca could take approximately one zeptosecond. As a consequence, the dynamical change of the density is most significant at low energy (near the barrier-top) where the colliding partners spend enough time in the vicinity of each other with little relative kinetic energy. At high energies, however, the nuclei overcome the barrier essentially in their ground-state density. This energy dependence of the effect of the couplings on the density evolution was clearly shown in TDHF calculations by Washiyama and Lacroix [87]. This naturally translates into an energy dependence of the nucleus-nucleus potential [88, 89], similar to what was introduced phenomenologically in the São-Paulo potential [90]. Consequently, the barrier corresponding to near barrier-top energies includes dynamical couplings effects and can be referred to as a *dynamic-adiabatic* barrier, while at high energy the nucleus-nucleus interaction is determined by a *sudden* potential which can be calculated assuming frozen ground-state densities.

In the DC-TDHF approach [91] the TDHF time-evolution takes place without any restrictions. At certain times during the evolution the instantaneous density is used to perform a static Hartree-Fock minimization while holding the neutron and proton densities constrained to be the corresponding instantaneous TDHF densities [92, 93]. In essence, this provides us with the TDHF dynamical path in relation to the multi-dimensional static energy surface of the combined nuclear system. The advantage of DC-TDHF in comparison to the frozen-density approximation of the previous section is obvious. The density is, in fact, not frozen, but polarized in the field of the neighbor fragment during collision. This is naturally taken into account in the TDHF prop-

agation and exactly mapped into an ion-ion potential in the DC-TDHF step. This time-dependent approach automatically incorporates static and dynamical polarization effects as there are neck formation, mass exchange, internal excitations, deformation effects to all orders, as well as the effect of nuclear alignment for deformed systems. In the DC-TDHF method the ion-ion interaction potential is given by

$$V_{DC}(R) = E_{\rm DC}(R) - E_{\rm A_1} - E_{\rm A_2} \ , \qquad (5)$$

where $E_{\rm DC}$ is the density-constrained energy at the instantaneous separation $R(t)$, while $E_{\rm A_1}$ and $E_{\rm A_2}$ are the binding energies of the two nuclei obtained with the same effective interaction. In writing Eq. (5) we have introduced the concept of an adiabatic reference state for a given TDHF state. The difference between these two energies represents the internal energy. The adiabatic reference state is the one obtained via the density constraint calculation, which is the Slater determinant with lowest energy for the given density with vanishing current and approximates the collective potential energy [92]. We would like to emphasize again that this procedure does not affect the TDHF time-evolution and contains no free parameters or normalization.

In addition to the ion-ion potential it is also possible to obtain coordinate dependent mass parameters. One can compute the "effective mass" $M(R)$ using the conservation of energy

$$M(R) = \frac{2[E_{\rm c.m.} - V_{DC}(R)]}{\dot{R}^2} \ , \qquad (6)$$

where the collective velocity $\dot{R}$ is directly obtained from the TDHF evolution and the potential $V_{DC}(R)$ from the density constraint calculations. In calculating fusion cross-sections this coordinate-dependent mass is used to obtain a transformed ion-ion potential $V(R)$ with an exact point-transformation as described in Ref. [94]. The coordinate dependent mass only modifies the inner part of the ion-ion potential and its importance was demonstrated in Ref. [88, 95]. Recently, the DC-TDHF method was employed for studying fusion reactions relevant for the neutron star crust [96, 97].

TDHF and DC-TDHF calculations were done in a three-dimensional Cartesian geometry with no symmetry assumptions and using the SV EDFs discussed above [98]. The three-dimensional Poisson equation for the Coulomb potential is solved by using Fast-Fourier Transform (FFT) techniques [99]. The static HF equations and the DC-TDHF minimizations are implemented by using the damped gradient iteration method [92, 93, 100, 101]. The box size used for the TDHF calculations in order to utilize the DC-TDHF method was chosen to be $60\times30\times30$ fm^3, with a mesh spacing of 1.0 fm in all directions. These values provide very accurate results due to the employment of sophisticated discretization techniques [99, 102]. In Fig. 5 we plot the ion-ion potentials for the ^{48}Ca+^{48}Ca system employing the DC-TDHF method. In this rather

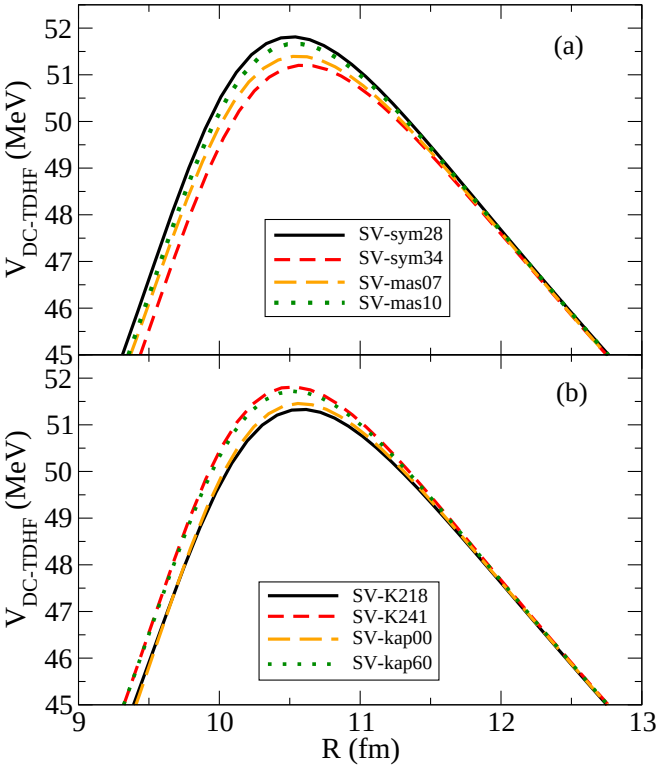

FIG. 5. (Color online) DC-TDHF ion-ion interaction potentials $V(R)$ for Skyrme SV EDFs; (a) potentials for SV-mas07, SV-mas10, SV-sym28, and SV-sym34. (b) potentials for SV-K218, SV-K241, SV-kap00, and SV-kap60.

expensive fully time-dependent approach, we have only calculated the potentials for the SV forces corresponding to the extreme values of the nuclear matter parameters. In Fig. 5(a) we plot the potentials for EDFs SV-sym28, SV-sym34, SV-mas07, and SV-mas10. Similar to the folding potentials we observe appreciable dependence on symmetry energy but little dependence on the effective mass, although there seems to be a bit more dependence in comparison to the folding-potential case. Figure 5(b) depicts the DC-TDHF potentials corresponding the EDFs SV-K216, SV-K241, SV-kap00, and SV-kap60. For these EDFs we see, again, an appreciable dependence on incompressibility but unlike the folding-potential case we see a stronger dependence on the value of $\kappa_{\rm TRK}$. This suggests that the dependence on $\kappa_{\rm TRK}$ is more sensitive to the dynamics such as the formation of a neck and particle transfer which, in fact, is not so surprising because $\kappa_{\rm TRK}$ is the dynamical isovector response parameter (see Appendix A).

The calculation of the fusion cross-sections using the DC-TDHF potentials employs the same IWBC approach used for the fusion cross-section calculations for double-folding potentials. Again, to better elucidate the dependence of fusion cross-sections on EDF parametrizations in Fig. 6 we plot the ratio of the calculated cross-sections corresponding to the potential barriers shown in Fig. 5 to the fusion cross-section of the SV-bas potential barrier as

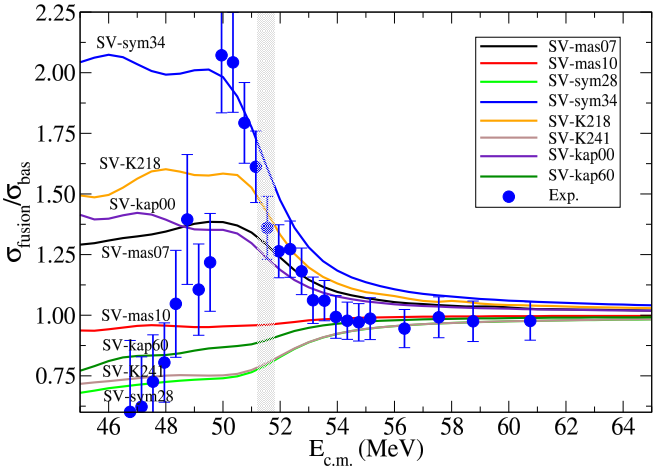

FIG. 6. (Color online) Fusion cross-sections corresponding to the DC-TDHF potentials $V(R)$ for Skyrme SV EDFs scaled with the cross-sections corresponding to the SV-bas EDF. The shaded area indicates the range of DC-TDHF potential barrier heights obtained using the SV forces. The experimental data, also scaled with the SV-bas cross-sections, (filled circles) are taken from Ref. [78] and include statistical as well as ±7% systematic error.

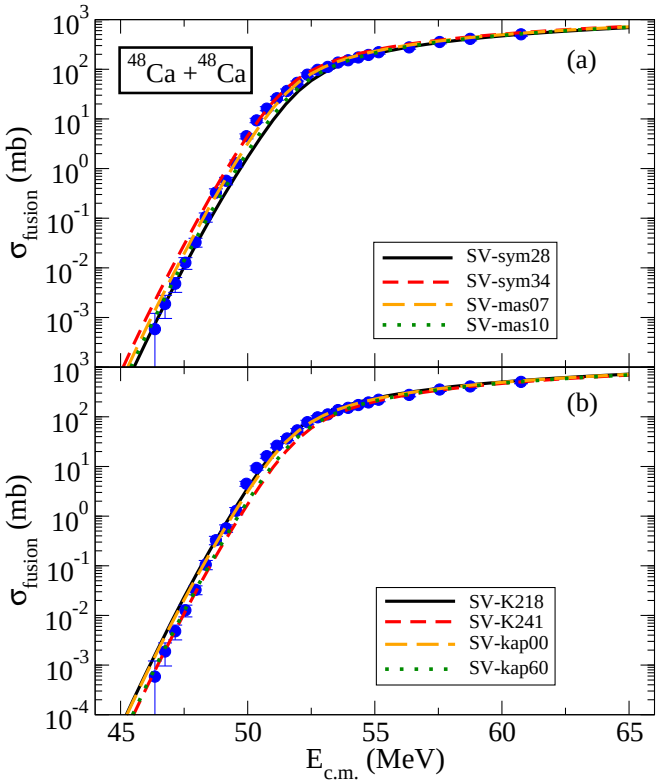

FIG. 7. (Color online) Fusion cross-sections corresponding to the DC-TDHF potentials $V(R)$ for Skyrme SV EDFs plot on a *log* scale; (a) cross-sections for SV-sym28, SV-sym34, SV-mas07, and SV-mas10. (b) cross-sections for SV-K218, SV-K241, SV-kap00, and SV-kap60. The experimental data (filled circles) are taken from Ref. [78].

a function of c.m. energy. The shaded area indicates the range of potential barrier heights for the potentials used in the study. We note that the dynamical barriers are 300−500 keV lower than the ones obtained from folding potentials. The experimental data [78] scaled also by the SV-bas cross-sections are shown as filled circles. A number of important points may be deduced from Fig. 6. We again observe that NMP corresponding to symmetry energy has the largest impact on the variation of the cross-sections. This is followed by incompressibility. A surprising observation is that the parameter κ induces a substantial variation in the cross-sections in this case, whereas it has practically no impact in the case of the folding potential approach. This indicates that the dynamics plays an important role in determining the important and correct NMP for nuclear reactions. What is also striking is that the parametrizations SV-mas10 and SV-kap60, and to a smaller extent SV-K241 and SV-sym28 provide an excellent description of the above barrier fusion data. However, at below barrier energies the dependence on NMP is much more complicated, namely a strong energy dependence.

Again, in Fig. 7 we plot the calculated fusion cross-sections on a logarithmic scale. Also shown are the experimental data (circles) from Ref. [78]. Before focusing on the details we observe that the DC-TDHF ion-ion potentials considerably improve the agreement with data at sub-barrier energies. This is due to the incorporation of neck dynamics in the construction of the potential, which modifies the inner part of the barrier. In fact the results are surprisingly good since the used EDFs do not include any reaction data for parameter fitting. One more important observation is that most DC-TDHF calculations to date have used the SLy4 [103] forces and one common discrepancy was always identified in the energy regime slightly above the barrier peak. We note that some of the SV forces, particularly SV-sym34 and SV-K218, seem to do a very good job in this regime but not as well at deep sub-barrier energies, where SV-sym28 and SV-K241 do better at these energies. It would be interesting to see if it is possible to construct an SV force which encompasses both nuclear matter values to see whether the complete energy regime can be reproduced. If we examine the DC-TDHF fusion cross-sections on a linear scale we again observe that the forces reproducing the barrier peak energy regime (SV-sym34, SV-mas07, SV-K218, SV-kap00) slightly overestimate the higher energy cross-sections whereas the forces that reproduce high energy cross-sections (SV-sym28, SV-mas10, SV-K241, SV-kap60) underestimate the barrier peak region.

The example shows that (dynamical) rearrangement of the colliding densities is crucial for a detailed reproduction of the fusion cross section. But the basic trends are already set by the folding model which relies exclusively on the neutron density distributions of the ground states of the colliding nuclei. And these densities are most sensitive to the density dependence of the symmetry energy.

In order to assess in a systematic fashion the sensitivity of the fusion cross section to the neutron-skin thickness of ^{48}Ca we have generated a set of "SV-L forces" that keep all NMP fixed at the SV-bas values and vary exclusively the slope of the symmetry energy L. In Fig. 8 we plot the potential barrier height for all of the forces used in this study. For the folding-model potentials we ob-

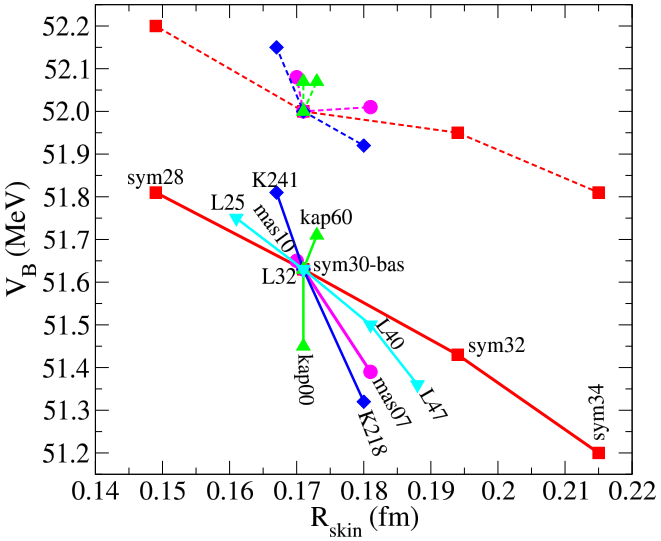

FIG. 8. (Color online) The maximum height of the potential energy barrier V_B as a function of the neutron skin $R_{\rm skin}$, as predicted by the set of systematically varied Skyrme parametrizations used in this paper. The dashed lines show the same quantities for the folding potentials.

serve an almost linear relationship between the neutron skin and the barrier height. This is expected since the densities are frozen. On the other hand, for the Skyrme parametrizations introduced in [59], we observe a more complicated behavior in our predictions, although at the extremes there is a clear sensitivity to the variations of the symmetry energy. We observe that each subset of parametrizations show a nearly linear trend with the provision that they have differing slopes. As expected, the systematically varied SV-L forces also display an almost linear correlation. In Fig. 9 we plot the SV parametrizations that best reproduce the data around the barrier top energies. We emphasize that these forces do reproduce the experimental data to a remarkable accuracy, with errors being on the order of a few millibarns. While it is not straightforward to pinpoint an unique set of NMP that provide the best agreement with the data, we observe that there is a tradeoff between having a stiff symmetry energy and a corresponding large neutron neutron-skin versus a softer symmetry energy and a somewhat smaller neutron-skin. Our analysis suggests a value for the symmetry energy closer to $J=30$ MeV with a relatively small neutron skin. Indeed, a neutron-skin thickness in ^{48}Ca of $R_{\rm skin}=(0.180-0.210)$ fm provides the optimal reproduction of the data.

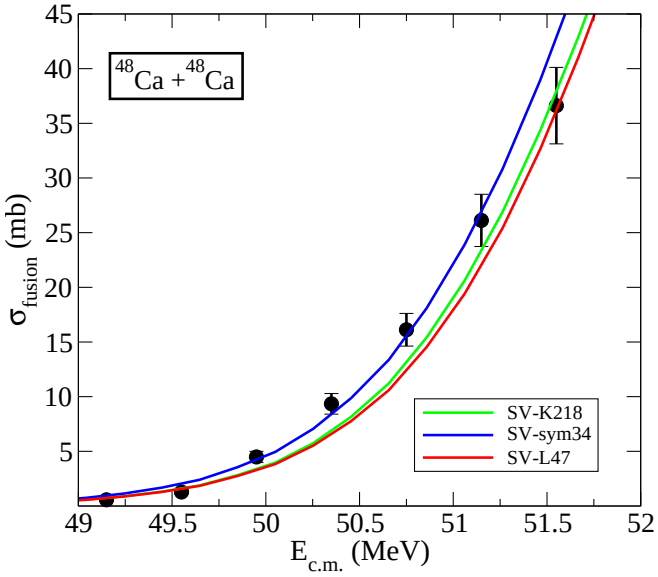

FIG. 9. (Color online) Fusion cross-sections in the vicinity of barrier top energies plotted for SV parametrizations that are most compatible with the fusion data in this energy regime.

C. Direct TDHF calculations

In the case of direct TDHF calculations of fusion cross sections the situation is different because they do not include sub-barrier tunneling of the many-body wavefunction. That is, the fusion probability, $P_{fus.}(L,E_{\rm c.m.})$, for a particular orbital angular momentum L at the center-of-mass energy $E_{\rm c.m.}$ can only be either $P_{fus.}^{TDHF}=0$ or 1. As a consequence, the quantal expression for the fusion cross-section

$$\sigma_{fus.}(E_{\rm c.m.})=\frac{\pi\hbar^2}{2\mu E_{\rm c.m.}}\sum_{L=0}^{\infty}(2L+1)P_{fus.}(L,E_{\rm c.m.})\ , \quad (7)$$

reduces to

$$\sigma_{fus.}(E_{\rm c.m.})=\frac{\pi\hbar^2}{2\mu E_{\rm c.m.}}\sum_{L=0}^{L_{max}(E_{\rm c.m.})}(2L+1)$$
$$=\frac{\pi\hbar^2}{2\mu E_{\rm c.m.}}[L_{max}(E_{\rm c.m.})+1]^2\ . \quad (8)$$

Here μ is the reduced mass of the system and L_{max} is the largest value of the orbital angular momentum leading to fusion. This is known as the quantum sharp cut-off formula [104].

To calculate the fusion cross-section within TDHF it is necessary to make many TDHF calculations to map out the maximum impact parameter for each energy of interest. We restrict our direct TDHF calculations to explore the systematic variation of the symmetry energy, since these showed the largest dependence in the DC-TDHF calculations. Figure 10 shows the calculated and experimental cross-sections for the SV-sym28, SV-bas, and SV-sym34 forces, with symmetry energies 28 MeV, 30 MeV,

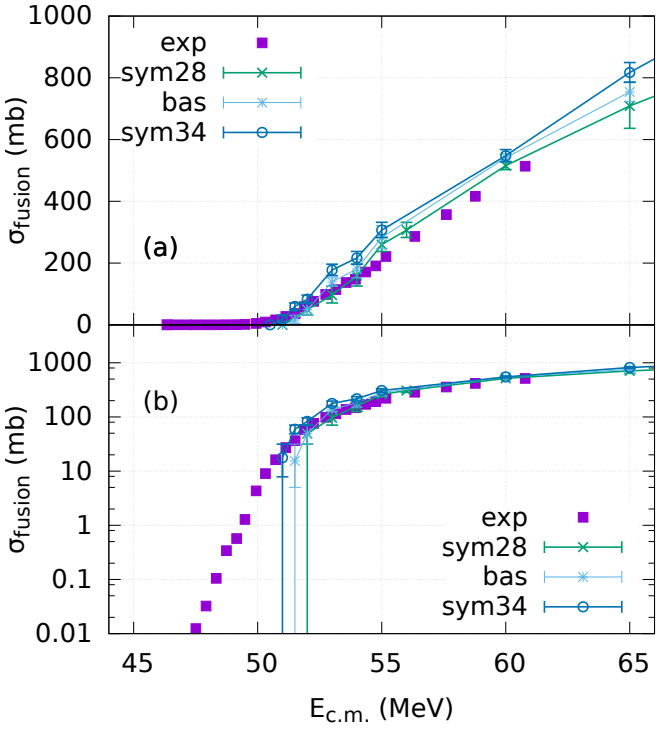

FIG. 10. (Color online) Cross-sections calculated directly from TDHF with SV-bas, SV-sym28, and SV-sym34. The panel (a) shows the data on a plot with a linear y–axis and panel (b) shows the same data with a logarithmic y–axis. The experimental data (filled circles) are taken from Ref. [78].

and 34 MeV respectively. The error bars associated with the calculations show the accuracy of determination of the critical impact parameter for each energy point indicated.

One notices that the results show the same systematic trends as the DC-TDHF calculations, namely, a softer symmetry energy gives a lower cross section. In particular, the force with a symmetry energy of $J = 28$ MeV seems to be slightly favored by the experimental data when the collision energy is greater than about 55 MeV, whereas models with a stiffer symmetry energies agree better near the barrier. The inability of direct TDHF calculations to reproduce the fusion cross section below the barrier is evident from the logarithmic plot, where the transition to zero cross section is seen for all forces in the region between 51 and 52 MeV center of mass energy.

IV. SUMMARY AND DISCUSSION

Elucidating the nature of the nuclear force that binds protons and neutrons into stable nuclei and rare isotopes is one of the overarching questions in nuclear science. In this paper we focused on the role that sub-barrier fusion may play in constraining the neutron density of ^{48}Ca, and in particular its neutron-rich skin. Being dominated by quantum-mechanical tunneling, the sub-barrier fusion of two ^{48}Ca nuclei is expected to be dominated by the spatial extent of its neutron distribution. This expectation was convincingly validated in this work. Indeed, models that predict a small neutron skin in ^{48}Ca delay the impact of the nuclear attraction to smaller values of the ion-ion separation causing an increase in the height of the Coulomb barrier relative to models with larger neutron skins. As a result, we have established the following correlation: the larger the neutron-skin thickness of ^{48}Ca, the larger the ^{48}Ca+^{48}Ca sub-barrier fusion cross section. Based on the limited set of systematically varied Skyrme forces employed in this work, our results seem to favor a slope for the symmetry energy of $L \approx 50\,\text{MeV}$ and a corresponding neutron-skin thickness in ^{48}Ca of $R_{\text{skin}} = (0.180-0.210)\,\text{fm}$.

The determination of the neutron-skin thickness of a variety of nuclei with a significant neutron excess provides critical information on the poorly-known isovector sector of the nuclear energy density functional. In turn, constraining the isovector sector determines the equation of state of neutron-rich matter, particularly the density dependence of the symmetry energy. The EOS of neutron-rich matter provides a powerful bridge between nuclear physics and astrophysics. Indeed, models that predict a large neutron skin in heavy nuclei also tend to predict large neutron-star radii. This correlation emerges since the same pressure that pushes against surface tension to generate the neutron skin pushes against gravity to shape the stellar radius. Remarkably, this correlation involves a disparity in length scales of 18 orders of magnitude! In this contribution we find another compelling connection between nuclear physics and astrophysics. Whereas sub-barrier fusion is hindered by the Coulomb barrier, the merger of two neutron stars is hindered by a large centrifugal barrier. Yet, the fusion of two neutron-rich nuclei or the merger of two neutron stars are both greatly enhanced by a stiff symmetry energy that produces large neutron skins and large stellar radii.

Ultimately, the most accurate determination of the neutron-skin thickness of ^{48}Ca will come from CREX—a parity-violating experiment that relies exclusively on the electro-weak nature of the electron probe. Yet, even under the most optimistic scenarios CREX is several years down the road. In the meantime, it is fruitful to explore complimentary approaches that probe similar physics. In this contribution we have established—in spite of some inherent hadronic uncertainties—that ^{48}Ca+^{48}Ca fusion near the Coulomb barrier is an attractive complement to CREX because of the exponential sensitivity of the reaction to the spatial distribution of neutrons.

ACKNOWLEDGMENTS

This material is based upon work supported by the U.S. Department of Energy Office of Science, Office of Nuclear Physics under Award Numbers DE-SC0013847

and DE-FD05-92ER40750, by the German BMBF under contract No. 05P12RFFTG, and by the UK Science and Technology Facilities Council (STFC) under grant numbers ST/J00051/1, ST/J500768/1, and ST/M503824/1.

Appendix A: Skyrme EDF and nuclear matter parameters (NMP)

For simplicity, we only discuss here the part of the Skyrme EDF containing the time-even couplings. The total energy is composed from kinetic energy, Skyrme interaction energy, Coulomb energy, pairing energy, and correlation energy from low-energy collective modes, usually a center-of-mass and a rotational correlation

$$E_{\rm total} = \int d^3r \ \{\mathcal{E}_{\rm kin} + \mathcal{E}_{\rm Sk}\} + E_{\rm Coul} + E_{\rm pair} - E_{\rm corr} \quad ,$$

with

$$\mathcal{E}_{\rm kin} = \frac{\hbar^2}{2m_p}\tau_p + \frac{\hbar^2}{2m_n}\tau_n \quad , \tag{A1}$$

and

$$\begin{aligned} \mathcal{E}_{\rm Sk} \ = \ & C_0^\rho \, \rho_0^2 && + \ C_1^\rho \, \rho_1^2 \\ & + C_0^{\rho,\alpha} \, \rho_0^{2+\alpha} && + \ C_1^{\rho,\alpha} \, \rho_1^2 \rho_0^\alpha \\ & + C_0^{\Delta\rho} \, \rho_0 \Delta\rho_0 && + \ C_1^{\Delta\rho} \, \rho_1 \Delta\rho_1 \\ & + C_0^{\nabla J} \, \rho_0 \nabla\cdot\vec{J}_0 && + \ C_1^{\nabla J} \, \rho_1 \nabla\cdot\vec{J}_1 \\ & + C_0^{\tau} \, \rho_0 \tau_0 && + \ C_1^{\tau} \, \rho_1 \tau_1 \\ & + C_0^{J} \, \vec{J}_0^2 && + \ C_1^{J} \, \vec{J}_1^2 \end{aligned} \tag{A2}$$

where ρ_T is the local density, τ_T the kinetic-energy density, $\vec{J}$ the spin-orbit density, and $T = 0, 1$ stands for isospin.

Infinite nuclear matter is taken without Coulomb force, pairing, and correlation correction. The energy per particle becomes

$$\frac{E}{A}(\rho_0, \rho_1, \tau_0, \tau_1) = \frac{\mathcal{E}_{\rm kin} + \mathcal{E}_{\rm Sk}}{\rho_0} \quad , \tag{A3}$$

where we consider for a while ρ and τ as independent variables. Of course, a given system is characterized just by the densities ρ_T while the kinetic density depends on these given densities as $\tau_T = \tau_T(\rho_0, \rho_1)$. Thus we have to distinguish between partial derivatives ∂/∂_τ which take τ_T as independent and total derivatives $d/d\rho$ which deal only with ρ_T dependence. The relation is

$$\frac{d}{d\rho_T} = \frac{\partial}{\partial\rho_T} + \sum_{T'} \frac{\partial\tau_{T'}}{\partial\rho_T}\frac{\partial}{\partial\tau_{T'}} \quad . \tag{A4}$$

The standard NMP are defined at the equilibrium point ($\rho_0 = \rho_{\rm eq}$, $\rho_1 = 0$) of symmetric nuclear matter. They are summarized in Table I. The enhancement factor for the Thomas-Reiche-Kuhn (TRK) sum rule [105] is a widely used way to characterize the isovector effective mass which is obvious from the given expression involving derivative with respect to τ_1. The slope of symmetry energy L characterizes the density dependence of the symmetry energy which allows to estimate the symmetry energy at half density, i.e. at surface of finite nuclei.

isoscalar ground state properties		
equilibrium density:	$\rho_{\rm eq} \leftrightarrow$	$\frac{d}{d\rho_0}\frac{E}{A}\Big\vert_{\rm eq} = 0$
equilibrium energy:		$\frac{E}{A}\Big\vert_{\rm eq}$
isoscalar response properties		
incompressibility:	$K_\infty \ =$	$9\,\rho_0^2 \frac{d^2}{d\rho_0^2}\frac{E}{A}\Big\vert_{\rm eq}$
effective mass:	$\frac{\hbar^2}{2m*} \ =$	$\frac{\hbar^2}{2m} + \frac{\partial}{\partial\tau_0}\frac{E}{A}\Big\vert_{\rm eq}$
isovector response properties		
symmetry energy:	$J \ =$	$\frac{1}{2}\frac{d^2}{d\rho_1^2}\frac{E}{A}\Big\vert_{\rm eq}$
slope of J:	$L \ =$	$\frac{3}{2}\rho_0\frac{d}{d\rho_0}\frac{d^2}{d\rho_1^2}\frac{E}{A}\Big\vert_{\rm eq}$
TRK sum-rule enh.:	$\kappa_{\rm TRK} \ =$	$\frac{2m}{\hbar^2}\frac{\partial}{\partial\tau_1}\frac{E}{A}\Big\vert_{\rm eq}$

TABLE I. Definition of the nuclear matter properties (NMP). All derivatives are to be taken at the equilibrium point of symmetric nuclear matter.

The NMP in Table I can be grouped into four classes: first, the (isoscalar) ground state properties $\rho_{\rm eq}$ and $E/A\Big\vert_{\rm eq}$, second, isoscalar response properties K and m^*/m, and third, isovector response properties J, L, $\kappa_{\rm TRK}$. The response properties determine zero sound in matter [106] and subsequently they are closely related to giant resonance modes in finite nuclei. There is a further category, the surface energies which go already beyond homogeneous matter and whose definition is rather involved [36]. They are not considered here.

Homogeneous matter yields $\Delta\rho = 0$ and $\vec{J} = 0$ which, in turn, renders four terms in the functional (A2) inactive. Thus we have exactly seven interaction parameters (C_0^ρ, $C_0^{\rho,\alpha}$, C_0^τ, α) to determine seven NMP. The relation is reversible establishing a one-to-one correspondence between both sets. This allows to consider the NMP equivalently as model parameters which is, in fact, a more intuitive way to ultimately determine the model parameters.

The fact that the NMP describes basic characteristics of a nuclear EDF suggests that one should explore an EDF by systematic variation of the NMP in the vicin-

Force	K	m^*/m	J	κ	$\rho_{\rm eq}$	E/A	L	Skin ^{208}Pb	Skin ^{48}Ca
SV-bas	234	0.9	30	0.4	0.1596	-15.90	32	0.155	0.171
SV-K218	218	0.9	30	0.4	0.1615	-15.90	35	0.161	0.180
SV-K226	226	0.9	30	0.4	0.1605	-15.90	34	0.159	0.176
SV-K241	241	0.9	30	0.4	0.1588	-15.91	31	0.151	0.167
SV-mas10	234	1.0	30	0.4	0.1594	-15.91	28	0.152	0.170
SV-mas08	234	0.8	30	0.4	0.1597	-15.90	40	0.160	0.175
SV-mas07	234	0.7	30	0.4	0.1500	-15.89	52	0.152	0.181
SV-sym28	234	0.9	28	0.4	0.1595	-15.86	7	0.117	0.149
SV-sym32	234	0.9	32	0.4	0.1595	-15.94	57	0.192	0.194
SV-sym34	234	0.9	34	0.4	0.1592	-15.97	81	0.227	0.215
SV-kap00	234	0.9	30	0.0	0.1598	-15.90	40	0.158	0.171
SV-kap20	234	0.9	30	0.2	0.1597	-15.90	36	0.155	0.170
SV-kap60	234	0.9	30	0.6	0.1595	-15.91	29	0.154	0.173
SV-L25	233.5	0.9	30	0.4	0.1596	-15.91	25	0.143	0.161
SV-L32	233.3	0.9	30	0.4	0.1594	-15.90	32	0.154	0.171
SV-L40	233.3	0.9	30	0.4	0.1594	-15.90	40	0.166	0.181
SV-L47	233.4	0.9	30	0.4	0.1596	-15.90	47	0.177	0.188

TABLE II. Nuclear matter parameters as defined in Ref. [59] for the various EDF parametrizations used in this paper (K in MeV, J in MeV, E/A in MeV, $\rho_{\rm eq}$ in fm^{-3}, L in MeV, m^*/m dimensionless, and $\kappa_{\rm TRK}$ dimensionless). As an observable from the finite nucleus, the neutron skin $R_n - R_p$ in ^{208}Pb and ^{48}Ca has been added in the last column (in units of fm).

ity of the values for the optimum EDF. This had been worked in detail in [59] delivering a set of systematically varied Skyrme parametrizations. As explained in Sec. II, we are using this set here for exploration of fusion. The detailed EDF parameters are given in [59]. Table II summarizes the NMP for the members of this set.

[1] A. B. Balantekin, J. Carlson, D. J. Dean, G. M. Fuller, R. J. Furnstahl, M. Hjorth-Jensen, R. V. F. Janssens, B.-A. Li, W. Nazarewicz, F. M. Nunes, W. E. Ormand, S. Reddy, and B. M. Sherrill, Mod. Phys. Lett. A **29**, 1430010 (2014).
[2] C. F. von Weizsäcker, Z. Phys. A **96**, 431 (1935).
[3] H. A. Bethe and R. F. Bacher, Rev. Mod. Phys. **8**, 82 (1936).
[4] J. Piekarewicz, Eur. Phys. J. A **50**, 25 (2014).
[5] W.-C. Chen and J. Piekarewicz, Phys. Rev. C **90**, 044305 (2014).
[6] P. Danielewicz, R. Lacey, and W. G. Lynch, Science **298**, 1592 (2002).
[7] M. B. Tsang, Y. Zhang, P. Danielewicz, M. Famiano, Z. Li, W. G. Lynch, and A. W. Steiner, Phys. Rev. Lett. **102**, 122701 (2009).
[8] P. Haensel and J. L. Zdunik, Astron. Astrophys. **229**, 117 (1990).
[9] N. Chamel and P. Haensel, Living Rev. Relat. **11** (2008).
[10] C. J. Horowitz, M. A. Pérez-García, and J. Piekarewicz, Phys. Rev. C **69**, 045804 (2004).
[11] R. Utama, J. Piekarewicz, and H. B. Prosper, Phys. Rev. C **93**, 014311 (2016).
[12] P. Bonche and D. Vautherin, Nucl. Phys. A **372**, 496 (1981).
[13] G. Watanabe, H. Sonoda, T. Maruyama, K. Sato, K. Yasuoka, and T. Ebisuzaki, Phys. Rev. Lett. **103**, 121101 (2009).
[14] G. Shen, C. J. Horowitz, and S. Teige, Phys. Rev. C **83**, 035802 (2011).
[15] J. Piekarewicz, Phys. Rev. C **76**, 064310 (2007).
[16] V. Baran, M. Colonna, V. Greco, and M. Di Toro, Phys. Rep. **410**, 335 (2005).
[17] A. W. Steiner, M. Prakash, J. M. Lattimer, and P. Ellis, Phys. Rep. **411**, 325 (2005).
[18] C. J. Horowitz, E. F. Brown, Y. Kim, W. G. Lynch, R. Michaels, A. Ono, J. Piekarewicz, M. B. Tsang, and H. H. Wolter, J. Phys. G. **41**, 093001 (2014).
[19] Bao-An Li and Àngels Ramos and Giuseppe Verde and Isaac Vidaña, Eur. Phys. J. A **50**, 1 (2014).
[20] B. Alex Brown, Phys. Rev. Lett. **85**, 5296 (2000).
[21] R. Furnstahl, Nucl. Phys. A **706**, 85 (2002).
[22] M. Centelles, S. K. Patra, X. Roca-Maza, B. K. Sharma, P. D. Stevenson, and X. Vinas, J. Phys. G **37**, 075107 (2010).
[23] X. Roca-Maza, M. Centelles, X. Viñas, and M. Warda, Phys. Rev. Lett. **106**, 252501 (2011).
[24] H. D. Vries, C. D. Jager, and C. D. Vries, Atom. Data Nucl. Data Tabl. **36**, 495 (1987).
[25] G. Fricke, C. Bernhardt, K. Heilig, L. Schaller, L. Schellenberg, E. Shera, and C. Dejager, Atomic Data and Nuclear Data Tables **60**, 177 (1995).
[26] I. Angeli and K. Marinova, At. Data Nucl. Data Tables **99**, 69 (2013).

[27] S. Abrahamyan, Z. Ahmed, H. Albataineh, K. Aniol, D. S. Armstrong, W. Armstrong, T. Averett, B. Babineau, A. Barbieri, V. Bellini, R. Beminiwattha, J. Benesch, F. Benmokhtar, T. Bielarski, W. Boeglin, A. Camsonne, M. Canan, P. Carter, G. D. Cates, C. Chen, J.-P. Chen, O. Hen, F. Cusanno, M. M. Dalton, R. De Leo, K. de Jager, W. Deconinck, P. Decowski, X. Deng, A. Deur, D. Dutta, A. Etile, D. Flay, G. B. Franklin, M. Friend, S. Frullani, E. Fuchey, F. Garibaldi, E. Gasser, R. Gilman, A. Giusa, A. Glamazdin, J. Gomez, J. Grames, C. Gu, O. Hansen, J. Hansknecht, D. W. Higinbotham, R. S. Holmes, T. Holmstrom, C. J. Horowitz, J. Hoskins, J. Huang, C. E. Hyde, F. Itard, C.-M. Jen, E. Jensen, G. Jin, S. Johnston, A. Kelleher, K. Kliakhandler, P. M. King, S. Kowalski, K. S. Kumar, J. Leacock, J. Leckey, J. H. Lee, J. J. LeRose, R. Lindgren, N. Liyanage, N. Lubinsky, J. Mammei, F. Mammoliti, D. J. Margaziotis, P. Markowitz, A. McCreary, D. McNulty, L. Mercado, Z.-E. Meziani, R. W. Michaels, M. Mihovilovic, N. Muangma, C. Muñoz Camacho, S. Nanda, V. Nelyubin, N. Nuruzzaman, Y. Oh, A. Palmer, D. Parno, K. D. Paschke, S. K. Phillips, B. Poelker, R. Pomatsalyuk, M. Posik, A. J. R. Puckett, B. Quinn, A. Rakhman, P. E. Reimer, S. Riordan, P. Rogan, G. Ron, G. Russo, K. Saenboonruang, A. Saha, B. Sawatzky, A. Shahinyan, R. Silwal, S. Sirca, K. Slifer, P. Solvignon, P. A. Souder, M. L. Sperduto, R. Subedi, R. Suleiman, V. Sulkosky, C. M. Sutera, W. A. Tobias, W. Troth, G. M. Urciuoli, B. Waidyawansa, D. Wang, J. Wexler, R. Wilson, B. Wojtsekhowski, X. Yan, H. Yao, Y. Ye, Z. Ye, V. Yim, L. Zana, X. Zhan, J. Zhang, Y. Zhang, X. Zheng, and P. Zhu (PREX Collaboration), Phys. Rev. Lett. **108**, 112502 (2012).

[28] C. J. Horowitz, Z. Ahmed, C.-M. Jen, A. Rakhman, P. A. Souder, M. M. Dalton, N. Liyanage, K. D. Paschke, K. Saenboonruang, R. Silwal, G. B. Franklin, M. Friend, B. Quinn, K. S. Kumar, D. McNulty, L. Mercado, S. Riordan, J. Wexler, R. W. Michaels, and G. M. Urciuoli, Phys. Rev. C **85**, 032501 (2012).

[29] T. Donnelly, J. Dubach, and I. Sick, Nucl. Phys. A **503**, 589 (1989).

[30] K. Paschke, K. Kumar, R. Michaels, P. A.Souder, and G. M. Urciuoli, *PREX–II: Precision parity-violating measurement of the neutron skin of lead*, Tech. Rep. (Jefferson Lab, 2012).

[31] M. Centelles, X. Roca-Maza, X. Viñas, and M. Warda, Phys. Rev. Lett. **102**, 122502 (2009).

[32] J. Mammei, D. McNulty, R. Michaels, K. Paschke, S. Riordan, and P. A. Souder, *CREX: Parity–violating measurement of the weak charge distribution of ^{48}Ca to 0.02 fm accuracy*, Tech. Rep. (Jefferson Lab, 2013).

[33] G. Hagen, A. Ekstrom, C. Forssen, G. R. Jansen, W. Nazarewicz, T. Papenbrock, K. A. Wendt, S. Bacca, N. Barnea, B. Carlsson, C. Drischler, K. Hebeler, M. Hjorth-Jensen, M. Miorelli, G. Orlandini, A. Schwenk, and J. Simonis, Nature **12**, 186 (2016).

[34] Z. Lin and C. J. Horowitz, Phys. Rev. C **92**, 014313 (2015).

[35] J. Blaizot, J. Berger, J. Dechargé, and M. Girod, Nucl. Phys. A **591**, 435 (1995).

[36] P.-G. Reinhard, M. Bender, W. Nazarewicz, and T. Vertse, Phys. Rev. C **73**, 014309 (2006).

[37] M. N. Harakeh and A. van der Woude, *Giant Resonances : Fundamental High-frequency Modes of Nuclear Excitation* (Clarendon Press, Oxford, 2001).

[38] J. Blaizot, Phys. Rep. **64**, 171 (1980).

[39] J. Bartel, P. Quentin, M. Brack, C. Guet, and H.-B. Håakansson, Nucl. Phys. A **386**, 79 (1982).

[40] P.-G. Reinhard, Nucl. Phys. A **649**, 305c (1999).

[41] P.-G. Reinhard and W. Nazarewicz, Phys. Rev. C **81**, 051303 (2010).

[42] A. Tamii, I. Poltoratska, P. von Neumann-Cosel, Y. Fujita, T. Adachi, C. A. Bertulani, J. Carter, M. Dozono, H. Fujita, K. Fujita, K. Hatanaka, D. Ishikawa, M. Itoh, T. Kawabata, Y. Kalmykov, A. M. Krumbholz, E. Litvinova, H. Matsubara, K. Nakanishi, R. Neveling, H. Okamura, H. J. Ong, B. Özel-Tashenov, V. Y. Ponomarev, A. Richter, B. Rubio, H. Sakaguchi, Y. Sakemi, Y. Sasamoto, Y. Shimbara, Y. Shimizu, F. D. Smit, T. Suzuki, Y. Tameshige, J. Wambach, R. Yamada, M. Yosoi, and J. Zenihiro, Phys. Rev. Lett. **107**, 062502 (2011).

[43] J. Piekarewicz, B. K. Agrawal, G. Colò, W. Nazarewicz, N. Paar, P.-G. Reinhard, X. Roca-Maza, and D. Vretenar, Phys. Rev. C **85**, 041302 (2012).

[44] X. Roca-Maza, M. Brenna, G. Colò, M. Centelles, X. Viñas, B. K. Agrawal, N. Paar, D. Vretenar, and J. Piekarewicz, Phys. Rev. C **88**, 024316 (2013).

[45] D. M. Rossi, P. Adrich, F. Aksouh, H. Alvarez-Pol, T. Aumann, J. Benlliure, M. Böhmer, K. Boretzky, E. Casarejos, M. Chartier, A. Chatillon, D. Cortina-Gil, U. Datta Pramanik, H. Emling, O. Ershova, B. Fernandez-Dominguez, H. Geissel, M. Gorska, M. Heil, H. T. Johansson, A. Junghans, A. Kelic-Heil, O. Kiselev, A. Klimkiewicz, J. V. Kratz, R. Krücken, N. Kurz, M. Labiche, T. Le Bleis, R. Lemmon, Y. A. Litvinov, K. Mahata, P. Maierbeck, A. Movsesyan, T. Nilsson, C. Nociforo, R. Palit, S. Paschalis, R. Plag, R. Reifarth, D. Savran, H. Scheit, H. Simon, K. Sümmerer, A. Wagner, W. Waluś, H. Weick, and M. Winkler, Phys. Rev. Lett. **111**, 242503 (2013).

[46] T. Hashimoto, A. M. Krumbholz, P.-G. Reinhard, A. Tamii, P. von Neumann-Cosel, T. Adachi, N. Aoi, C. A. Bertulani, H. Fujita, Y. Fujita, E. Ganio, K. Hatanaka, E. Ideguchi, C. Iwamoto, T. Kawabata, N. T. Khai, A. Krugmann, D. Martin, H. Matsubara, K. Miki, R. Neveling, H. Okamura, H. J. Ong, I. Poltoratska, V. Y. Ponomarev, A. Richter, H. Sakaguchi, Y. Shimbara, Y. Shimizu, J. Simonis, F. D. Smit, G. Süsoy, T. Suzuki, J. H. Thies, M. Yosoi, and J. Zenihiro, Phys. Rev. C **92**, 031305(R) (2015).

[47] X. Roca-Maza, X. Viñas, M. Centelles, B. K. Agrawal, G. Colò, N. Paar, J. Piekarewicz, and D. Vretenar, Phys. Rev. C **92**, 064304 (2015).

[48] P.-G. Reinhard, Ann. Phys. (Leipzig) **504**, 632 (1992).

[49] N. Van Giai, P. F. Bortignon, G. Colò, Z.-Y. Ma, and M. Quaglia, Nuclear Physics A **687**, 44 (2001).

[50] P.-G. Reinhard, Lu Guo, and J. Maruhn, Eur. Phys. J. A **32**, 19 (2007).

[51] J. A. Maruhn, P. G. Reinhard, P. D. Stevenson, J. Rikovska Stone, and M. R. Strayer, Phys. Rev. C **71**, 064328 (2005).

[52] V. O. Nesterenko, W. Kleinig, J. Kvasil, P. Vesely, P.-G. Reinhard, and D. S. Dolci, Phys. Rev. C **74**, 064306 (2006).

[53] T. Nakatsukasa and K. Yabana, Phys. Rev. C **71**,

024301 (2005).
[54] A. S. Umar and V. E. Oberacker, Phys. Rev. C **71**, 034314 (2005).
[55] C. Simenel, P. Chomaz, and G. de France, Phys. Rev. Lett. **86**, 2971 (2001).
[56] C. Simenel and P. Chomaz, Phys. Rev. C **68**, 024302 (2003).
[57] D. Lacroix and P. Chomaz, Nucl. Phys. A **636**, 85 (1998).
[58] N. Paar, D. Vretenar, E. Khan, and G. Colò, Rep. Prog. Phys **70**, 691 (2007).
[59] P. Klüepfel, P.-G. Reinhard, T. J. Bürvenich, and J. A. Maruhn, Phys. Rev. C **79**, 034310 (2009).
[60] C. J. Horowitz and J. Piekarewicz, Phys. Rev. Lett. **86**, 5647 (2001).
[61] C. J. Horowitz and J. Piekarewicz, Phys. Rev. C **64**, 062802 (2001).
[62] J. Erler, C. J. Horowitz, W. Nazarewicz, M. Rafalski, and P.-G. Reinhard, Phys. Rev. C **87**, 044320 (2013).
[63] W. H. Dickhoff and H. Müther, Rep. Prog. Phys. **55**, 1947 (1992).
[64] V. R. Pandharipande, I. Sick, and P. K. A. deWitt Huberts, Rev. Mod. Phys. **69**, 981 (1997).
[65] E. Epelbaum, H.-W. Hammer, and U.-G. Meißner, Rev. Mod. Phys. **81**, 1773 (2009).
[66] R. Machleidt and D. R. Entem, Phys. Rep. **503**, 1 (2011).
[67] H.-W. Hammer, A. Nogga, and A. Schwenk, Rev. Mod. Phys. **85**, 197 (2013).
[68] M. Kortelainen, J. Erler, W. Nazarewicz, N. Birge, Y. Gao, and E. Olsen, Phys. Rev. C **88**, 031305 (2013).
[69] J. Dobaczewski, W. Nazarewicz, and P.-G. Reinhard, J. Phys. G **41**, 074001 (2014).
[70] J. Erler and P.-G. Reinhard, J. Phys. G **42**, 034026 (2014).
[71] P.-G. Reinhard, Phys. Scr. **91**, 023002 (2016).
[72] F. J. Fattoyev and J. Piekarewicz, Phys. Rev. C **84**, 064302 (2011).
[73] T. H. R. Skyrme, Phil. Mag. **1**, 1043 (1956).
[74] D. Vautherin and D. M. Brink, Phys. Rev. C **5**, 626 (1972).
[75] M. Bender, P. H. Heenen, and P.-G. Reinhard, Rev. Mod. Phys. **75**, 121 (2003).
[76] A. S. Umar and V. E. Oberacker, Phys. Rev. C **74**, 061601 (2006).
[77] R. Keser, A. S. Umar, and V. E. Oberacker, Phys. Rev. C **85**, 044606 (2012).
[78] A. M. Stefanini, G. Montagnoli, R. Silvestri, L. Corradi, S. Courtin, E. Fioretto, B. Guiot, F. Haas, D. Lebhertz, P. Mason, F. Scarlassara, and S. Szilner, Phys. Lett. B **679**, 95 (2009).
[79] H. Esbensen, C. L. Jiang, and A. M. Stefanini, Phys. Rev. C **82**, 054621 (2010).
[80] L. Ray, Phys. Rev. C **19**, 1855 (1979).
[81] G. R. Satchler and W. G. Love, Phys. Rep. **55**, 183 (1979).
[82] G. Bertsch, J. Borysowicz, H. Mcmanus, and W. G. Love, Nucl. Phys. A **284**, 399 (1977).
[83] M. J. Rhoades-Brown and V. E. Oberacker, Phys. Rev. Lett. **50**, 1435 (1983).
[84] M. J. Rhoades-Brown, V. E. Oberacker, M. Seiwert, and W. Greiner, Z. Phys. A **310**, 287 (1983).
[85] K. Hagino, N. Rowley, and A. T. Kruppa, Comput. Phys. Commun. **123**, 143 (1999).
[86] C. Simenel, M. Dasgupta, D. J. Hinde, and E. Williams, Phys. Rev. C **88**, 064604 (2013).
[87] Kouhei Washiyama and Denis Lacroix, Phys. Rev. C **78**, 024610 (2008).
[88] A. S. Umar, C. Simenel, and V. E. Oberacker, Phys. Rev. C **89**, 034611 (2014).
[89] X. Jiang, J. A. Maruhn, and S. Yan, Phys. Rev. C **90**, 064618 (2014).
[90] L. C. Chamon, B. V. Carlson, L. R. Gasques, D. Pereira, C. De Conti, M. A. G. Alvarez, M. S. Hussein, M. A. C. Ribeiro, E. S. Rossi, and C. P. Silva, Phys. Rev. C **66**, 014610 (2002).
[91] A. S. Umar and V. E. Oberacker, Phys. Rev. C **74**, 021601 (2006).
[92] R. Y. Cusson, P.-G. Reinhard, M. R. Strayer, J. A. Maruhn, and W. Greiner, Z. Phys. A **320**, 475 (1985).
[93] A. S. Umar, M. R. Strayer, R. Y. Cusson, P.-G. Reinhard, and D. A. Bromley, Phys. Rev. C **32**, 172 (1985).
[94] A. S. Umar and V. E. Oberacker, Eur. Phys. J. A **39**, 243 (2009).
[95] V. E. Oberacker, A. S. Umar, J. A. Maruhn, and P.-G. Reinhard, Phys. Rev. C **82**, 034603 (2010).
[96] A. S. Umar, V. E. Oberacker, and C. J. Horowitz, Phys. Rev. C **85**, 055801 (2012).
[97] C. Simenel, R. Keser, A. S. Umar, and V. E. Oberacker, Phys. Rev. C **88**, 024617 (2013).
[98] A. S. Umar and V. E. Oberacker, Phys. Rev. C **73**, 054607 (2006).
[99] J. A. Maruhn, P.-G. Reinhard, P. D. Stevenson, and A. S. Umar, Comp. Phys. Comm. **185**, 2195 (2014).
[100] A. S. Umar, M. R. Strayer, P.-G. Reinhard, K. T. R. Davies, and S.-J. Lee, Phys. Rev. C **40**, 706 (1989).
[101] C. Bottcher, M. R. Strayer, A. S. Umar, and P.-G. Reinhard, Phys. Rev. A **40**, 4182 (1989).
[102] A. S. Umar, M. R. Strayer, J. S. Wu, D. J. Dean, and M. C. Güçlü, Phys. Rev. C **44**, 2512 (1991).
[103] E. Chabanat, P. Bonche, P. Haensel, J. Meyer, and R. Schaeffer, Nucl. Phys. A **635**, 231 (1998).
[104] J. S. Blair, Phys. Rev. **95**, 1218 (1954).
[105] P. Ring and P. Schuck, *The Nuclear Many–Body Problem* (Springer–Verl., New York, Heidelberg, Berlin, 1980).
[106] D. J. Thouless, *The Quantum Mechanics of Many–Body Systems* (Academic Press, New York, 1961).